Solid Earth, 13, 745–759, 2022
https://doi.org/10.5194/se-13-745-2022

Solid Earth Open Access EGU

Thermal equation of state of the main minerals of eclogite: Constraining the density evolution of eclogite during the delamination process in Tibet

Zhilin Ye[1,2], Dawei Fan[1], Bo Li[3], Qizhe Tang[4], Jingui Xu[5], Dongzhou Zhang[5], and Wenge Zhou[1]

[1]Key Laboratory of High-Temperature and High-Pressure Study of the Earth's Interior, Institute of Geochemistry, Chinese Academy of Sciences, Guiyang, Guizhou 550081, China
[2]University of Chinese Academy of Sciences, Beijing 100049, China
[3]Research Institute of Petroleum Exploration & Development-Northwest (NWGI), PetroChina Lanzhou 730020, China
[4]School of Information Engineering, Huzhou University, Huzhou, Zhejiang 313000, China
[5]Hawaii Institute of Geophysics and Planetology, School of Ocean and Earth Science and Technology, University of Hawaii at Manoa, Honolulu, Hawaii 96822, USA

Correspondence: Dawei Fan (fandawei@vip.gyig.ac.cn) and Jingui Xu (xujingui@hawaii.edu)

Received: 15 September 2021 – Discussion started: 29 September 2021
Revised: 8 February 2022 – Accepted: 4 March 2022 – Published: 30 March 2022

Abstract. Tibet, which is characterized by collisional orogens, has undergone the process of delamination or convective removal. The lower crust and mantle lithosphere appear to have been removed through delamination during orogenic development. Numerical and analog experiments demonstrate that the metamorphic eclogitized oceanic subduction slab or lower crust may promote gravitational instability due to increased density. The eclogitized oceanic subduction slab or crustal root is believed to be denser than the underlying mantle and tends to sink. However, the density of eclogite under high-pressure and high-temperature conditions as well as density differences from the surrounding mantle are not preciously constrained. Here, we offer new insights into the derivation of eclogite density with a single experiment to constrain delamination in Tibet. Using in situ synchrotron X-ray diffraction combined with a diamond anvil cell, experiments focused on minerals (garnet, omphacite, and epidote) of eclogite are conducted under simultaneous high-pressure and high-temperature conditions, which avoids systematic errors. Fitting the pressure–temperature–volume data with the third-order Birch–Murnaghan equation of state, the thermal equation of state (EoS) parameters, including the bulk modulus (K_{T0}), its pressure derivative (K'_{T0}), and the thermal expansion coefficient (α_0), are derived. The densities of rock-forming minerals and eclogite are modeled along with the geotherms of two types of delamination. The delamination processes of subduction slab break-off and the removal of the eclogitized lower crust in Tibet are discussed. The Tibetan eclogite, which contains 40 vol %–60 vol % garnet and 44 %–70 % eclogitization, can promote the delamination of slab break-off in Tibet. Our results indicate that eclogite is a major controlling factor in the initiation of delamination. A high abundance of garnet, a high Fe content, and a high degree of eclogitization are more conducive to instigating the delamination.

1 Introduction

The evolution of orogenesis is characterized by lithospheric removal during rapid surface uplift, mantle upwelling, and post-collisional magmatism, particularly in the central Andes (e.g., Ehlers and Poulsen, 2009), Himalayas (e.g., Singh and Kumar, 2009), and Dabie orogen (e.g., He et al., 2011).

It is widely accepted that delamination is the most important mechanism of lithospheric removal. Delamination is induced and accompanied by two major requisites: (a) the density difference caused by the negative buoyancy of the delaminated lithosphere and (b) the presence of a weak lower crust (lower viscosity) that exists between the strong upper

crust and lithospheric mantle. Usually, two types of delamination are believed to occur in orogen development. The first is the conventional definition of delamination proposed by Bird (1978, 1979), which was used to interpret the geodynamic evolution of the Colorado Plateau. In this scenario, mantle lithosphere peels back from the overlying upper crust and is removed entirely, with the rising hot mantle filling the lithospheric removal zone (e.g., Göğüş and Ueda, 2018; Krystopowicz and Currie, 2013). A weak decoupling layer, i.e., the lower crust, is an essential condition in this delamination model, which may be affected by the rheological behavior of the hydration, thermal, and chemical characteristics of the lithosphere (e.g., Morency, 2004). In addition to conventional delamination, an alternative delamination mechanism is convective removal based on the Rayleigh–Taylor instability model (Houseman et al., 1981), namely viscous "dripping". This model postulates that there is sufficient perturbation in the lithospheric mantle, which is ascribed to the strong temperature dependence of typical mantle rheology, without regard to a specific weak layer (e.g., Conrad and Molnar, 1999; Houseman and McKenzie, 1982).

All previous studies attribute the gravitational instability process of lithospheric removal to the negative thermal buoyancy of the cold lithosphere (Conrad and Molnar, 1999; Houseman and McKenzie, 1982) or density contrast between the asthenosphere and mantle lithosphere. In any case, the density distribution with lithosphere pressure and temperature (P–T) conditions as well as chemical composition is of vital importance to understanding the process of lithospheric removal.

The Tibetan Plateau is the most representative and prominent collisional orogen. Two types of delamination are proposed to proceed (e.g., Chung et al., 2005; Houseman et al., 1981): lithospheric mantle removal and thickened eclogitized crust removal. The Neo-Tethyan oceanic subduction, India–Asia collision, and Indian continental subduction could be further considered to be responsible for the abnormal thinning of the mantle lithosphere under Tibet (Chung et al., 2005; Li et al., 2019). The lithospheric removal event in Tibet corresponds to Neo-Tethyan oceanic slab break-off. The mechanism is primarily based on density contrasts between the denser mantle lithosphere and the lighter underlying mantle. Some models reveal that lithospheric removal is induced by the retreating high-density eclogitized lithosphere detached from overlying low-density crust (Faccenda et al., 2009; Li et al., 2016). Other alternative models indicate that thickened eclogitized crust is a potential factor driving lithospheric removal because the eclogitized crustal root is denser than the underlying mantle and tends to sink (Krystopowicz and Currie, 2013). Regardless of the above types of delamination, the density of eclogite is closely related to delamination. Therefore, Tibet provides an excellent opportunity to understand the role of eclogite density in the process of delamination.

An immense amount of concrete research has focused on the origin and appearance of lithospheric mantle removal from different angles, such as geophysical (Ren and Shen, 2008), geological (Chung et al., 2005), petrological (Chung et al., 2005; Turner et al., 1993), and numerical and analog experiments (Göğüş and Pysklywec, 2008; Morency, 2004). In particular, numerical and analog experiments are used as prominent methods to simulate the dynamics of delamination (Göğüş and Ueda, 2018). Of these studies, the density behavior occurring during the delamination process has also been investigated intensively following thermodynamic (Semprich et al., 2010), seismic and/or tomography (Matchette-Downes et al., 2019), and numerical simulations (Li et al., 2016). However, few studies have systematically illuminated the issue of delamination from the perspective of eclogite density. Here, we attempt to offer new insights into the derivation of rock density through the mineral physics method to constrain delamination in Tibet (Ye et al., 2021). Conducting a single experiment under high-pressure and high-temperature conditions, we obtain the equation of state (EoS) of the main minerals of eclogite with fewer systematic errors in the experiment. Furthermore, the newly derived EoS of the main minerals of eclogite, combined with the published EoSs of the main minerals of peridotite (Ye et al., 2021), geothermal lines, and collected eclogite mineral compositions, is further used to elucidate a density evolution model during the delamination process in Tibet. We argue that the EoSs of minerals could be used in a straightforward manner as new constraints on the construction of the density model. Using a simplistic calculation setup, in this study, this density evolution model will shed light on the possibility of delamination during the orogen process.

2 Geological background

The Tibetan Plateau is composed of four terranes from south to north: the Himalaya, Lhasa, Qiangtang, and Songpan–Ganzi terranes (Fig. 1). The birth of the Himalayas and Tibetan Plateau is a consequence of the Indo-Asian collision, which began in the early Cenozoic (Hodges et al., 2001; Wang et al., 2008). The Neo-Tethyan oceanic slab is proposed to have detached from the Indian lithosphere, and the onset of the Indo-Asian collision (DeCelles et al., 2002) particularly occurred in the lower part of the Indian and Lhasa lithospheres. The tectonic evolutionary history of the Lhasa terrane and Tethys Himalayas is essential for revealing the origin of the Himalayan–Tibetan orogen. The subducting Neo-Tethyan slab was thrust into southern Tibet at approximately 70–65 Ma (Fig. 1b). With the closure of the Neo Tethyan Ocean, the India–Asia continent collision caused compressional deformation in southern Tibet, and a series of collision break-off events were delineated spanning from 65 to 42 Ma (Chung et al., 2005, 2009; Ma et al., 2014; Zhu et al., 2015). During this period, the Indian continen-

tal lithosphere might have been dragged down to deeper depths during subduction. Meanwhile, slab rollback accompanied by the southward migration of asthenospheric convection in Tibet changed the thermal structure of the mantle wedge. The break-off of the oceanic Neo-Tethyan slab from the more buoyant Indian continental lithosphere indicated by the eruption of early Eocene Linzizong volcanic rocks in the Gangdese arc or the cessation of Gangdese arc magmatism occurred at ∼ 45 Ma (DeCelles et al., 2002), which opened a channel for the upwelling asthenosphere (Chung et al., 2009; Ma et al., 2014; Zhu et al., 2015). Additionally, geophysical evidence of longitudinal wave (V_P) tomography is interpreted for the north-dipping high-speed anomaly, which is ascribed to the deep Indian mantle lithosphere (Li et al., 2008). Subsequently, the subduction of the Indian continental margin continues at a low subduction angle beneath the Lhasa terrane (Guillot et al., 2008).

In addition, 25 to 0 Ma is another period considered to contain either the occurrence of slab break-off (Miller et al., 1999) or lithospheric mantle removal following slab break-off (Chung et al., 2005; Nomade et al., 2004). Previous studies suggested that the hotter asthenosphere considerably raised the geothermal conditions during this period (Chung et al., 2005). Ultra-potassic, shoshonitic, and calc–alkaline magmatism was widespread, which was potentially due to the partial melts of the metasomatized lithospheric mantle and eclogitized lower crust. An adopted model of convective lithospheric removal below Lhasa is widely followed (Miller et al., 1999). The lithospheric removal-related mantle upwelling process has been supported by geological, geophysical, and petrological studies (Chung et al., 2005; Ren and Shen, 2008; Turner et al., 1993).

Here, slab break-off and convective lithospheric removal under Tibet are adopted as the background in this study to discuss the possibility of the delamination process.

3 Materials and methods

3.1 Starting material

Natural garnet, omphacite, and epidote samples are collected from eclogite in the Dabie–Sulu ultrahigh-pressure metamorphic (UHPM) belt. The compositions of each mineral are determined to be $Prp_{21}Alm_{47}Grs_{31}Sps_1$ (Prp: pyrope, Alm: almandine, Grs: grossular, and Sps: spessartine) for garnet, $Quad_{48}Jd_{45}Ae_7$ (Quad: ferrosilite + enstatite + wollastonite, Jd: jadeite, Ae: aegirine) for omphacite, and $Ca_{2.02}Fe_{0.75}Al_{2.32}Si_{0.16}[SiO_4][Si_2O_7]O(OH)$ for epidote. The compositions of garnet and omphacite are shown in Fig. 2 and are within the range of natural mineral compositions of eclogite from Tibet. The chemical composition of representative epidote minerals in Tibet shows that the Fe content of epidote exposed in eclogite is in the range of 0.13–0.25 ($X_{Fe} = Fe^{3+}/(Fe^{3+} + Al^{3+})$) (Huang et al., 2015; Li et al., 2017; Liu et al., 2016), while the Fe content of epidote in this study is 0.24, which is within the Fe content range of natural epidote. The samples used in this study are representative of garnet, omphacite, and epidote minerals in natural eclogites from Tibet. The garnet, omphacite, and epidote with high-quality grains are separated from the eclogite specimens. The above three samples are crushed into 30 µm × 40 µm chips with a single-crystal thickness of 15 µm in our experiment.

3.2 Synchrotron X-ray diffraction

The high-pressure and high-temperature experiment is conducted by using a BX90 externally heated diamond anvil cell (EHDAC) with ±15° opening angles. The above three single crystals are loaded into the BX90 EHDAC equipped with a pair of 500 µm culet-sized diamond anvils and tungsten carbide (WC) seats (Fig. S1 in the Supplement). The rhenium (Re) gasket is pre-indented to a thickness of ∼ 60 µm, and a cylindrical hole with a diameter of 360 µm is drilled as a sample chamber. Gold powder is also loaded as the pressure calibrant (Fei et al., 2007), and neon is loaded as the pressure-transmitting medium through the GeoSoilEnviroCARS (GSECARS) gas-loading system (Rivers et al., 2008). The quasi-hydrostatic condition in the sample chamber can be maintained up to ∼ 20 GPa using the neon pressure-transmitting medium (Finkelstein et al., 2017). On the other hand, high temperature can significantly decrease the deviatoric stress conditions in the sample chamber. Moreover, previous studies demonstrate that the deviatoric stress disappears at the temperatures of 650 K with neon as the pressure-transmitting medium (Klotz et al., 2009; Meng et al., 1993). Therefore, the hydrostatic and quasi-hydrostatic conditions can be maintained within the P–T range of our experiment (∼ 700 K, 25 GPa). An automated pressure-driven membrane system is utilized to generate increasing pressure up to 25.6 GPa. High-temperature conditions up to 700 K are provided by the heating resistor. Before collecting data, the temperature in the sample chamber is stabilized for 5 min and the temperature fluctuation is less than 1 K. Setup details for the employed thermocouples and heaters can be found in our previous articles (Xu et al., 2019, 2020b; Ye et al., 2021).

In situ synchrotron single-crystal X-ray diffraction (XRD) experiments were performed at experimental station 13-BM-C of the Advanced Photon Source, Argonne National Laboratory. The detailed experimental process and associated parameters can be seen in our previous studies (Xu et al., 2017, 2018, 2020a; Zhang et al., 2017). The diffraction images and the lattice parameters were analyzed by the Bruker APEX3 software package (Dera et al., 2013). The representative single-crystal X-ray diffraction patterns are shown in Fig. S2 in the Supplement. The specific unit cell parameters of the above three samples at each P–T condition can be found in Table S1 in the Supplement.

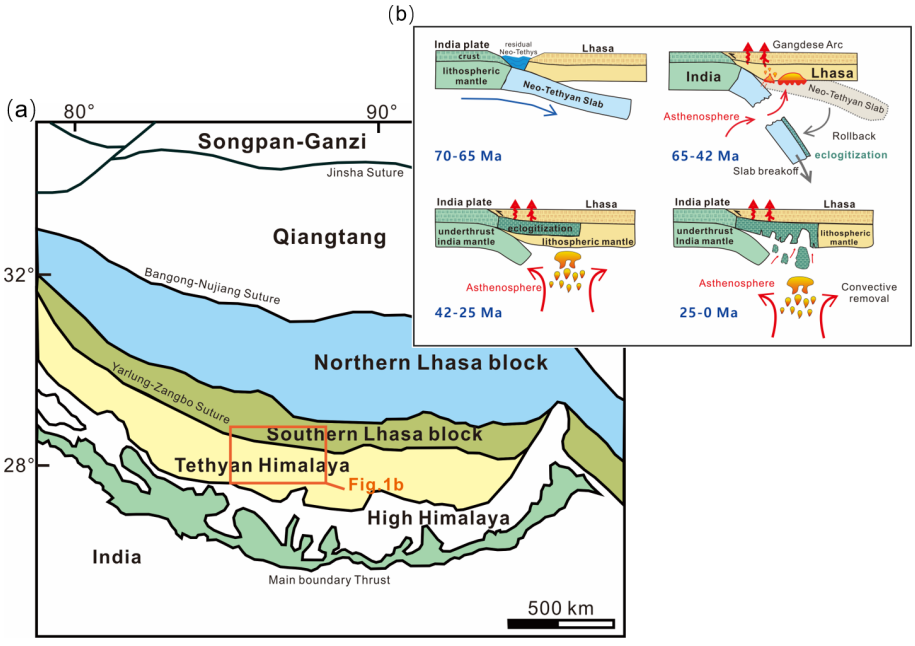

Figure 1. (a) Schematic geological map of the Tibetan Plateau (modified from Chung et al., 2005, and Wang et al., 2010). **(b)** Interpretive geological cartoon of India–Asia collision evolution. 70–65 Ma: the flat Neo-Tethyan oceanic slab subducts beneath Tibet with the closure of the Neo-Tethys Ocean. 65–42 Ma: the rollback of the Neo-Tethyan slab breaks off after densification by eclogitization. 42–25 Ma: the subduction of the Indian continent continued at a low subduction angle beneath the Lhasa terrane and was accompanied by heavy thermal perturbation. 25–0 Ma: the thickened eclogitic lower crust undergoes the "convective removal" of delamination due to gravitational instability.

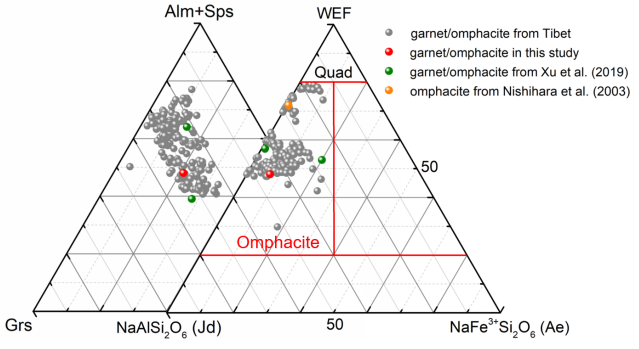

Figure 2. Composition of garnet and omphacite in eclogites from Tibet and this study. The gray solid circles represent the components of garnet and omphacite collected from previous studies in Tibet (e.g., Chan et al., 2009; Liu et al., 2019; Song et al., 2003; Weller et al., 2016; Yang et al., 2009; Zhai et al., 2011a). The green solid circles are garnet and omphacite with different Fe contents according to Xu et al. (2019). The orange solid circles are omphacite according to Nishihara et al. (2003). The red solid circles are the components of garnet and omphacite in this study. Prp: pyrope, Alm: almandine, Grs: grossular, Sps: spessartine, Quad: ferrosilite + enstatite + wollastonite, Jd: jadeite, and Ae: aegirine.

4 Results and discussion

4.1 EoS of main minerals for eclogite

The pressure–volume–temperature (P–V–T) data in this study are fitted by the third-order Birch–Murnaghan EoS (BM3-EoS) (Birch, 1947) in combination with the Holland–Powell thermal pressure EoS (Holland and Powell, 2011) to obtain the thermal EoS parameters. The volume is calculated in P–T space starting with an isothermal compression and followed by a path along an isochor curve to the final temperature. The pressure at a given volume and temperature consists of the following two parts:

$$P(V,T) = P(V,T_0) + P_{\mathrm{th}}(V,T), \tag{1}$$

The first term corresponds to the pressure calculated by the BM3-EoS for compression at room temperature (T_0). The zero-pressure volume (V_{T0}), the isothermal bulk modulus (K_{T0}), and its pressure derivate (K'_{T0}) have the following form:

$$P(V,T_0) = \frac{3}{2}K_{T0}\left[\left(\frac{V_{T0}}{V}\right)^{\frac{7}{3}} - \left(\frac{V_{T0}}{V}\right)^{\frac{5}{3}}\right] \times \left\{1 + \frac{3}{4}(K'_{T0}-4)\left[\left(\frac{V_{T0}}{V}\right)^{\frac{2}{3}} - 1\right]\right\}. \tag{2}$$

The second term is the additional pressure generated by heating along an isochor. The thermal pressure follows the equation

$$P_{\mathrm{th}}(V,T) = \alpha_{V,0} K_{T0} \left(\frac{\theta_{\mathrm{E}}}{\xi_0}\right) \times \left(\frac{1}{\exp\left(\frac{\theta_{\mathrm{E}}}{T}\right)-1} - \frac{1}{\exp\left(\frac{\theta_{\mathrm{E}}}{T_0}\right)-1}\right), \quad (3)$$

where $\xi = (\theta_{\mathrm{E}}/T)^2 \exp(\theta_{\mathrm{E}}/T)/((\theta_{\mathrm{E}}/T)-1)^2$, ξ_0 is the value of ξ at the reference temperature T_0, and $\alpha_{V,0}$ is the thermal expansion coefficient at room temperature. The Einstein temperature θ_{E} in this study is selected and recalculated from the literature (Faccincani et al., 2021; Gottschalk, 2004).

The thermal EoS parameters are derived using the EoSFit program at high-pressure and room-temperature conditions as well as at high-pressure and high-temperature conditions (Angel et al., 2014) and are shown in Table S2 in the Supplement. Under ambient pressure and temperature conditions, the measured V_0 values of garnet, omphacite, and epidote are 1566.05 (25) $\mathrm{Å}^3$, $V_0 = 423.48$ (24) $\mathrm{Å}^3$, and $V_0 = 461.57$ (23) $\mathrm{Å}^3$, respectively. The fitting parameters under high pressure and at room temperature yield $K_{T0} = 170$ (1) GPa, and $K'_{T0} = 3.74$ (22) for garnet, $K_{T0} = 121(2)$ GPa, and $K'_{T0} = 3.90$ (35) for omphacite, and $K_{T0} = 122(1)$ GPa, and $K'_{T0} = 2.51$ (16) for epidote.

To evaluate the quality of BM3-EoS fitting in this study, the relationship between the Eulerian strain ($f_{\mathrm{E}} = [(V_0/V)^{2/3} - 1]$) and the normalized pressure ($F_{\mathrm{E}} = P/[3 f_{\mathrm{E}}(2 f_{\mathrm{E}} + 1)^{5/2}]$) of the main minerals for eclogite is plotted in Fig. S3 in the Supplement. Linear fitting of the three sets of data exhibited a negative slope, indicating that the pressure derivative of the bulk modulus (K'_{T0}) is less than 4, which is consistent with our BM3-EoS fittings. The intercept value was obtained by weighted linear regression of the data points, showing that $F_{\mathrm{E}}(0) = 171$ (2) GPa for garnet, $F_{\mathrm{E}}(0) = 123$ (2) for omphacite, and $F_{\mathrm{E}}(0) = 122$ (1) for epidote. The results are consistent with the fitted isothermal bulk modulus ($K_{T0} = 170$ (1) GPa for garnet, $K_{T0} = 121$ (2) GPa for omphacite, and $K_{T0} = 122$ (1) GPa for epidote) within the error range. Accordingly, the K_{T0} and K'_{T0} obtained by the BM3-EoS fitting are reasonable. Using the V_0 fixed at ambient conditions to fit third-order Birch–Murnaghan and Holland–Powell thermal pressure EoS (BM3-HP-EoS), the available EoS parameters are derived: $K_{T0} = 170$ (1) GPa, $K'_{T0} = 3.82$ (14), and $\alpha_0 = 2.71$ (5) $\times 10^{-5}\,\mathrm{K}^{-1}$ for garnet; $K_{T0} = 121$ (3) GPa, $K'_{T0} = 3.97$ (34), and $\alpha_0 = 3.73(20) \times 10^{-5}\,\mathrm{K}^{-1}$ for omphacite; and $K_{T0} = 124$ (2) GPa, $K'_{T0} = 2.04$ (15), and $\alpha_0 = 3.04$ (13) $\times 10^{-5}\,\mathrm{K}^{-1}$ for epidote. The P–V–T data fitted through the BM3-HP-EoS model are shown in Fig. 3.

4.2 Comparison with previous studies

4.2.1 Garnet

The thermal EoS parameters of garnet are obtained by fitting the P–V–T data to the BM3-EoS. We compare our results with those of previous studies (Arimoto et al., 2015; Gréaux and Yamada, 2014; Lu et al., 2013; Milani et al., 2015, 2017; Xu et al., 2019; Zou et al., 2012). The K_{T0} of end-member garnet, pyrope, almandine, grossular, and spessartine crystals is between 158 and 179 GPa, and the bulk modulus of almandine is the largest among the above (Table S3 in the Supplement). From Table S3, it can be seen that the bulk modulus of powder XRD (Arimoto et al., 2015; Gréaux and Yamada, 2014; Pavese et al., 2001; Zou et al., 2012) is larger than those of single-crystal XRD (Milani et al., 2015, 2017) with the same composition. The K_{T0} of solid solution garnets (Beyer et al., 2021; Jiang et al., 2004; Lu et al., 2013; Xu et al., 2019) is also between 158 and 179 GPa, as mentioned above, and will be affected by the end-member components. The $K_{T0} = 170$ (1) GPa in this study is reasonable within this range. The obtained $K'_{T0} = 3.82$ (14) in this study is slightly lower than that in previous studies. The Eulerian strain and the normalized pressure of the garnet shown in Fig. S3a exhibit a negative slope, indicating that K'_{T0} is less than 4. Moreover, compared with the previous results, the obtained value of K'_{T0} in this study is within the error range (Sect. S1 in the Supplement). However, there is no obvious correlation between the fitted K_{T0} and K'_{T0} for minerals of different compositions (Fig. S4 in the Supplement); hence, the K_{T0} may not be precise when K'_{T0} is fixed. For the α_0, the andradite has the largest value ($3.16(2) \times 10^{-5}\,\mathrm{K}^{-1}$), and the grossular has the smallest value ($2.09\ (2) \times 10^{-5}\,\mathrm{K}^{-1}$) among the end-member garnets. The thermal expansion coefficient of $\mathrm{Prp}_{21}\mathrm{Alm}_{47}\mathrm{Grs}_{31}\mathrm{Sps}_1$ ($2.71\ (5) \times 10^{-5}\,\mathrm{K}^{-1}$) in this study is comparable with previous studies, but the influence of composition still needs to be considered.

4.2.2 Omphacite

Many studies have focused on the thermoelastic properties of omphacite (Hao et al., 2019; Nishihara et al., 2003; Pandolfo et al., 2012a, b; Xu et al., 2019; Zhang et al., 2016) (Table S3). Most of the results are obtained by the single-crystal XRD method, except for the result of Nishihara et al. (2003), which was obtained from powder XRD. K'_{T0} shows a higher value of 6.9 (12) in the study of Nishihara et al. (2003), while in others, K'_{T0} is between 4 and 5.7, and the result of K'_{T0} (3.97) in this study is slightly lower than the above values. Additionally, according to the results shown in Table S3, the bulk moduli of omphacite are in the range of 115–123 GPa. In the study of Xu et al. (2019), an increase in the iron content would decrease K_{T0}, and they also discussed the reasons for the discrepancy in K_{T0} in detail, such as the effective ionic radius, pressure-transmitting

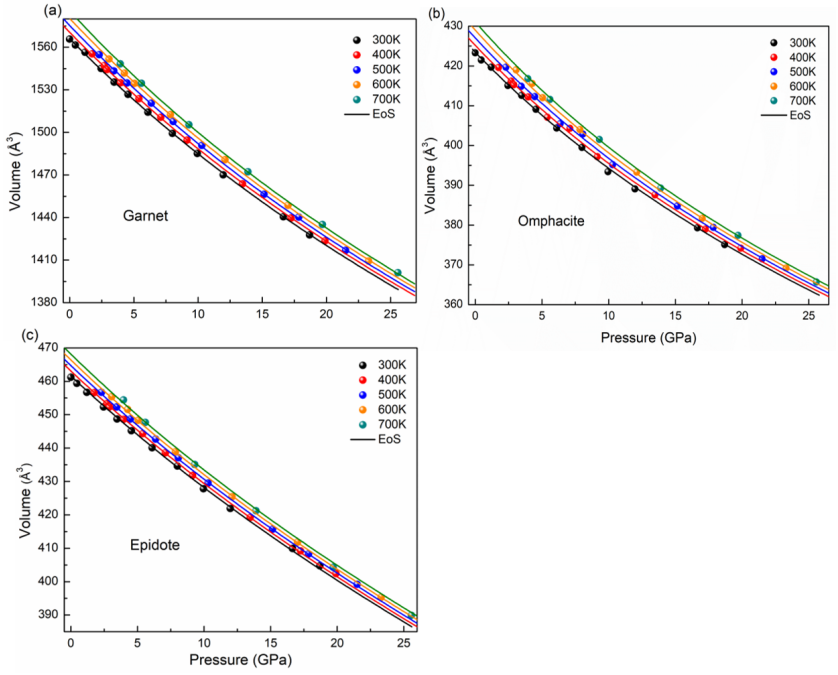

Figure 3. Pressure–volume–temperature relations of garnet **(a)**, omphacite **(b)**, and epidote **(c)**. Isothermal compression curves are calculated by using the thermoelastic parameters obtained in this study.

medium, and experimental pressure range. Comparing our results with Xu et al. (2019), we conclude that the incorporation of Fe would reduce the bulk modulus. However, except for Fe content, there does not seem to be a significant correlation between the other components and the bulk modulus of omphacite. The α_0 of the Di–Jd solid solution is similar ($2.64\ (2) \times 10^{-5}$–$2.8\ (3) \times 10^{-5}\ K^{-1}$) but less than that of $Quad_{48}Jd_{45}Ae_7$ ($3.73\ (20) \times 10^{-5}\ K^{-1}$) and $Quad_{53}Jd_{27}Ae_{20}$ ($3.4\ (4) \times 10^{-5}\ K^{-1}$). It may be inferred that the Ae contents affect thermal expansion.

4.2.3 Epidote

The thermal EoS parameters of epidote in this study are compared with those reported in previous studies (Fan et al., 2014; Gatta et al., 2011; Holland et al., 1996; Li et al., 2020; Qin et al., 2016) (Table S3). Although the bulk modulus appears to be related to the Fe^{3+} content, it does not show a good correlation. Increasing the content of Fe^{3+} can enhance the bulk modulus, but the result in Holland et al. (1996) shows an abnormally large value of 162 (4) GPa, which is much higher than the 111–133 GPa resulting from other studies. This may be attributed to the fixed K'_{T0} at 4 and powder XRD methods used in the study of Holland et al. (1996). Furthermore, the K'_{T0} obtained from powder XRD (Fan et al., 2014; Gatta et al., 2011) is also larger than that from single-crystal XRD (Qin et al., 2016). The possible reasons for these discrepancies are complicated. Li et al. (2020) conducted a detailed study on this topic. Previous studies on α_0 and $(\partial K_T/\partial T)_P$ of epidote are limited. The α_0 ($3.04\ (13) \times 10^{-5}\ K^{-1}$) in this study is lower than that of Gatta et al. (2011) ($5.1\ (2) \times 10^{-5}\ K^{-1}$) and Li et al. (2020) ($3.8\ (5) \times 10^{-5}\ K^{-1}$).

5 Implications

In the Himalayan–Tibetan system, lithospheric removal is proposed to occur in either the break-off of the subducted slab of the Indian continental lithosphere (Chung et al., 2005; Turner et al., 1993) or convective removal of the thickened lower part of the lithosphere (Miller et al., 1999). The metamorphic eclogitization taking place in the subducted slab and the lowermost crust has been deduced as the possible cause of subducted slab break-off and the convective removal of the lower crust (Krystopowicz and Currie, 2013). Increased density in the eclogitized subducted slab and the lower crust will promote the above two lithospheric removal modes if the lower crust is weak enough for the negative buoyancy of the mantle lithosphere to be detached. Therefore, to better consider the role of eclogite density variations in the process of lithospheric removal, we model the density of minerals and eclogite aggregates along with the geotherms of Tibet and discuss the effects of the degree of eclogitization on lithospheric removal.

The eclogite chemical data collected in Tibet and examined in our study come from a great number of eclogite samples collected in previous studies (e.g., Chan et al., 2009; Liu

et al., 2019; Yang et al., 2009; Zhai et al., 2011a). The eclogite samples consist of garnet, omphacite, epidote, amphibole, zoisite, and symplectite along with minor phengite, quartz, and rutile, as well as rare apatite, ilmenite, and titanite as accessory minerals. Since the eclogite samples have suffered retrograde metamorphism, we assume that they are largely composed of garnet and omphacite plus slight epidote before retrograde metamorphism. The accessory phases observed in natural eclogite are excluded because of their minimal abundance of less than 5 %. Based on the mineral composition data on exposed eclogite in Tibet (Fig. S6 in the Supplement) (e.g., Cheng et al., 2015; Dong et al., 2018; Huang et al., 2015; Jin et al., 2019; Li et al., 2017; Zhai et al., 2011a, b), the components of eclogite are 50 vol % garnet + 45 vol % omphacite + 5 vol % epidote (parameterized as a value out of 100) using the normal distribution.

We take into account two different delamination modes, namely delamination caused by the separation of the Neo-Tethyan slab (detachment of the subducted Neo-Tethyan oceanic slab) in the Paleozoic and convective removal of the lower crust of the subducted Indian continent beneath the Lhasa terrane during the Cenozoic. The temperature and pressure conditions of exposed eclogites in the Paleozoic and Cenozoic are somewhat consistent with the geothermal lines provided by previous studies (Fig. S7 in the Supplement). The two different delamination modes reflect relatively cold geotherms and hot geotherms, respectively. Therefore, these geothermal lines are used in our models. The thermal EoS parameters of eclogitic garnet, omphacite, and epidote are derived through the BM3-HP-EoS shown in Table S2.

5.1 The density of main minerals for eclogite along the geothermal profile in Tibet

Tibetan eclogite is mainly composed of garnet and omphacite, with a few epidotes. As shown in Fig. 2, the exposed minerals differ in composition. The specific composition of minerals constrains the density. Therefore, we refer to the thermoelastic parameters of Xu et al. (2019) and Nishihara et al. (2003) to depict the density distribution of different components (Fe content) of garnet and omphacite under Tibetan geothermal lines, respectively. The corresponding thermoelastic parameters can be seen in Table S3. The mineral compositions of previous studies are within the range of the Tibetan constituents collected in this study (Fig. 2).

The density distribution of minerals along with relatively cold Tibetan geothermal conditions is shown in Fig. 4 (the results along with hot geotherms can be seen in Fig. S8 in the Supplement). The result clearly shows that the density of garnet is linked with the iron content. The density of garnet ($Prp_{21}Alm_{47}Grs_{31}Sps_1$, with 47 mol % almandine) in this study is higher than that of low-Fe garnet ($Prp_{28}Alm_{38}Grs_{33}Sps_1$, with 38 mol % almandine) (Xu et al., 2019) by 2.22 % but lower than that of high-Fe garnet ($Prp_{14}Alm_{62}Grs_{19}Adr_3Sps_2$, with 62 mol % almandine) (Xu et al., 2019) by 3.82 % at $\sim$ 80 km (Fig. 4a). With increasing depth, the density of high-Fe garnet increases by a larger amplitude. This discrepancy may be caused by its smaller degree of thermal expansion ($2.56(44) \times 10^{-5}\,K^{-1}$). Accordingly, the influence of pressure on the density is greater than that of temperature, which leads to faster increases in density with depth. The density of omphacite does not show obvious characteristics related to its composition. The density of omphacite ($Quad_{48}Jd_{45}Ae_7$, with 7 mol % aegirine) in this study is lower than that of high-Fe omphacite ($Quad_{53}Jd_{27}Ae_{20}$, with 20 mol % aegirine) (Xu et al., 2019), $Quad_{72}Jd_{28}$ (Nishihara et al., 2003), and $Quad_{57}Jd_{42}Ae_1$ (with 1 mol % aegirine) (Xu et al., 2019) by 1.95 %, 1.47 %, and 0.83 %, respectively, at $\sim$ 80 km (Fig. 4b). The presence of iron in certain quantities does increase the density of omphacite, but the density of omphacite is also affected by other elements, such as calcium and magnesium. Moreover, thermal EoS parameters are also of vital importance to calculate the density. The relatively low thermal expansion of $Quad_{72}Jd_{28}$ ($2.7(3) \times 10^{-5}\,K^{-1}$) and $Quad_{57}Jd_{42}Ae_1$ (with 1 mol % aegirine) ($2.8(3) \times 10^{-5}\,K^{-1}$) may further enhance the increasing rate of density with depth. It is worth noting that the densities of $Quad_{48}Jd_{45}Ae_7$ (with 7 mol % aegirine) in this study and $Quad_{57}Jd_{42}Ae_1$ (with 1 mol % aegirine) in Xu et al. (2019) are the same under ambient conditions but inconsistent under high-pressure and high-temperature conditions. Therefore, the K_{T0} and K'_{T0} of the two omphacites are somewhat consistent with each other, while the thermal expansion and $(\partial K_T/\partial T)_P$ are different. Collectively, the thermal EoS parameters are of the essence in the derivation of the mineral density.

5.2 The density of eclogite in Tibet

Eclogitized crust and lithospheric mantle may be potential factors causing delamination (Faccenda et al., 2009; Krystopowicz and Currie, 2013). The density of eclogite and peridotite can provide new constraints to control the break-off of the subducted slab and convective removal of the lithosphere in the process of delamination. Therefore, we plot the density distribution of eclogite with different garnet contents and peridotite along the Paleozoic and Cenozoic Tibetan geotherms, as shown in Fig. 5. In our model, the mineral composition of Tibetan eclogite is in the range of 40 vol % garnet + 55 vol % omphacite + 5 vol % epidote to 60 vol % garnet + 35 vol % omphacite + 5 vol % epidote based on the exposed eclogite in Tibet (the composition of epidote is only 5 vol % by default due to its low content in this study). The composition of surrounding peridotite consists of 70 vol % olivine + 25 vol % orthopyroxene + 3 vol % clinopyroxene + 2 vol % spinel (Yang et al., 2019; Zhao et al., 2021). The densities of eclogite and peridotite aggregates are obtained considering their arithmetic mean. The densities of each mineral under specific temperature and pressure conditions are

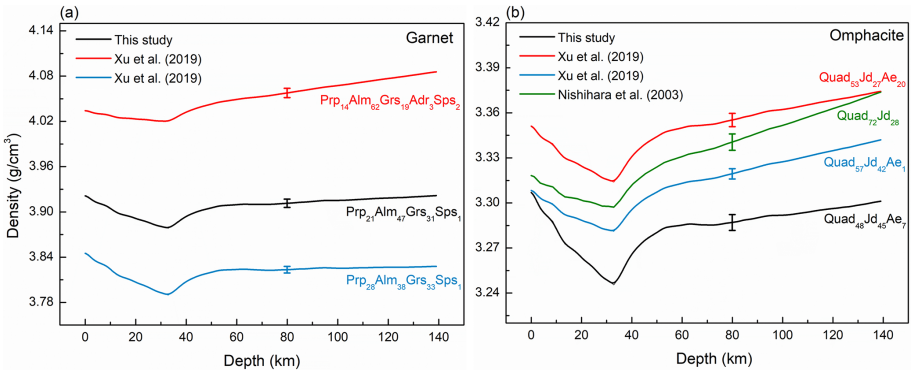

Figure 4. Density profiles of garnet **(a)** and omphacite **(b)** along with the cold Tibetan geothermal line (Wang et al., 2013). The garnets of $Prp_{21}Alm_{47}Grs_{31}Sps_1$ and $Prp_{28}Alm_{38}Grs_{33}Sps_1$ are from Xu et al. (2019). The omphacites of $Quad_{53}Jd_{27}Ae_{20}$ and $Quad_{57}Jd_{42}Ae_1$ are from Xu et al. (2019), and $Quad_{72}Jd_{28}$ is from Nishihara et al. (2003).

derived by the following formula:

$$\rho\,(T,P) = \frac{V\,(T,0)}{V\,(T,P)} \times \frac{Z \times M}{N_{\mathrm{a}} \times V_0}, \tag{4}$$

where V_0 is the reference unit cell volume at ambient conditions, M is molecular weight, Z is the number of formula units in the unit cell, and N_{a} is the Avogadro number.

Most changes in the deep conditions of the Earth progress slowly, so there is adequate time for recrystallization to relieve the maximum stress point (Robertson, 1988; Skinner, 1966). Here, we assume that the elastic–plastic interaction among different minerals and possible deviations from hydrostatic conditions are ignored, and the density of the eclogite aggregate can be obtained by the arithmetic mean as follows:

$$\overline{\rho} = \sum \lambda_i \rho_i\,(T,P)\,, \tag{5}$$

where the subscript i denotes the ith mineral of the upper mantle, and λ is the volume proportion of each mineral.

The densities of Tibetan eclogite (with the garnet composition of $Prp_{21}Alm_{47}Grs_{31}Sps_1$, the omphacite composition of $Quad_{48}Jd_{45}Ae_7$, and the epidote composition of $Ca_{2.02}Fe_{0.75}Al_{2.32}Si_{0.16}(SiO_4)(Si_2O_7)O(OH)$) and peridotite (with the olivine composition of $Fo_{89.9}Fa_{10.1}$, the orthopyroxene composition of $En_{89.6}Fs_{9.7}Wo_{0.7}$, the clinopyroxene composition of $Quad_{88.5}Jd_{11.5}$, and the spinel composition of $(Mg_{0.790}Fe_{0.204}Ni_{0.005}Ti_{0.001})_{1.000}(Al_{0.821}Cr_{0.158}Fe_{0.021})_{2.002}O_4$) in this study along the Paleozoic geothermal line are shown in Fig. 5a. The results show that the increase in garnet has a profound influence on the density of eclogite. For every 10 % increase in garnet, the density of eclogite increases by $\sim$ 1.7 %. The garnet content in Tibetan eclogite is estimated to be 40 vol %–60 vol % (Fig. S6). The densities of this part of eclogite are 3.54–3.66 g cm^{-3}, which is approximately 7.4 %–11.2 % more than that of peridotite (3.29 g cm^{-3}) at $\sim$ 80 km. The density difference between eclogite and peridotite is 0.24–0.37 g cm^{-3} (Fig. 5b). At the same time, we also consider the density of eclogite aggregates without epidote (Fig. S6). The results show that 5 vol % epidote has little effect on the density of eclogite, especially eclogite with garnet contents of 50 vol %–60 vol % (Fig. S9 in the Supplement). To account for the role of iron, the density distributions of high-Fe ($Prp_{14}Alm_{62}Grs_{19}Adr_3Sps_2$ and $Quad_{53}Jd_{27}Ae_{20}$) and low-Fe eclogite ($Prp_{28}Alm_{38}Grs_{33}Sps_1$ and $Quad_{57}Jd_{42}Ae_1$) are plotted to better constrain the range of eclogite density (Fig. S10 in the Supplement) (Xu et al., 2019). For high-Fe and low-Fe eclogites, the densities of eclogite increase by $\sim$ 1.9 % and $\sim$ 1.4 % for each 10 % increase in garnet, respectively. The densities of eclogite are 3.64–3.78 g cm^{-3} for high Fe content and 3.53–3.63 g cm^{-3} for low Fe content at $\sim$ 80 km. Furthermore, the densities of high-Fe and low-Fe eclogites are 10.6 %–14.9 % and 7.2 %–10.3 % higher than the surrounding peridotite, respectively. For a more straightforward comparison, taking eclogite containing 50 vol % garnet as an example (Fig. S11 in the Supplement), the densities of high-Fe eclogite, low-Fe eclogite, and Tibetan eclogite at $\sim$ 80 km are 3.71, 3.58, and 3.61 g cm^{-3}, respectively. An increase in the iron content can substantially increase the density of eclogite, although it will be constrained by the thermal EoS parameters of minerals.

Similarly, we also discuss the density profile along the Cenozoic geothermal line, which can be seen in Sect. S2 in the Supplement. In any case, the density difference caused by eclogite may be one of the prominent factors instigating the delamination process.

5.3 Influence of the degree of eclogitization on the density of the subducted slab

Eclogite in the mantle, which is believed to be 5 %–10 % denser than peridotite (Garber et al., 2018), is responsible for the excess compositional density. Furthermore, some calculations propose that the degree of eclogitization of the subducted slab is a key factor in the delamination process (Matchette-Downes et al., 2019). To investigate the influence

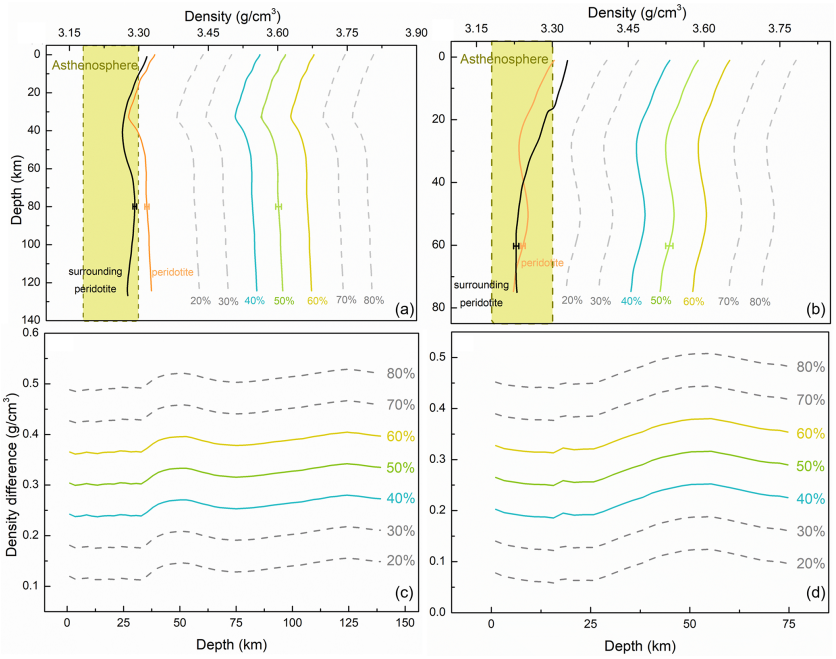

Figure 5. Density profiles of eclogite and peridotite assemblages **(a** and **b)** the density difference between eclogite and peridotite **(c** and **d)** in Tibet along the Paleozoic and Cenozoic geothermal lines under the conditions of Neo-Tethyan oceanic slab detachment **(a)** (Wang et al., 2013) as well as subduction of the Indian continental margin beneath the Lhasa terrane **(b)** (Craig et al., 2020). The percentage represents the content of garnet in eclogite, of which epidote accounts for 5 vol % by default. The orange curve and black curves show the density profile of peridotite with a composition of 70 vol % olivine + 25 vol % orthopyroxene + 3 vol % clinopyroxene + 2 vol % spinel. The orange line shows the density of peridotite in the lithospheric mantle along the Paleozoic **(a)** (Wang et al., 2013) and Cenozoic **(b)** (Craig et al., 2020) geothermal lines, and the black curve indicates that the density of peridotite in the surrounding lithospheric mantle is along the Paleozoic **(a)** (Nábělek and Nábělek, 2014) and Cenozoic **(b)** (Wang et al., 2013) geothermal lines in Tibet. The shaded region is the density range of the asthenosphere (Chen and Tenzer, 2019; Levin, 2006; Panza et al., 2020; Singh and Mahatsente, 2020).

of the degree of eclogitization in the delamination process, we plot the density variations with different mineral compositions under different degrees of eclogitization (Fig. 6). We consider eclogitization in the lithospheric mantle of the subducted slab; here the degree of eclogitization refers to the amount of eclogite in the lithospheric mantle. In our preferred model, the 7 km thick subducted oceanic crust becomes eclogite, while the lithospheric mantle constrains a different amount of eclogite. Since the subducted Indian oceanic slab might be fragmented into several pieces, the longitudinal size of the fractured slab is postulated to be 60 km (Peng et al., 2016). Our estimated average density of the fragmented slab with various degrees of eclogitization is shown in Fig. 6a. The results clearly show that the density increases monotonically with the garnet content and the degree of eclogitization. The garnet content is of profound importance to the density of eclogite. The higher the proportion of garnet is, the more the density increases with increasing degrees of eclogitization. The garnet content in Tibetan eclogite is estimated to be between 40 vol % and 60 vol %. Taking garnet with an average volume percentage of 50 vol % in Tibetan eclogite as an example, the density of eclogitized subducted slabs ranges from 3.35 g cm^{-3} with 10 % eclogitization to 3.61 g cm^{-3} with 100 vol % eclogitization. For a garnet content of 50 vol %, the density increases by 0.029 g cm^{-3} per 10 vol % increase in the degree of eclogitization. The density will increase with increasing garnet contents from 0.006 g cm^{-3} for 10 vol % to 0.051 g cm^{-3} for 90 vol %. The densities of high-Fe and low-Fe eclogitized fragmented slabs are also shown in Fig. S12 in the Supplement. The high Fe content shows that the density variation increases with the degree of eclogitization from 0.007 g cm^{-3} for 10 vol % to 0.064 g cm^{-3} for 90 vol % garnet, while the low Fe content shows a density change from 0.004 g cm^{-3} for 10 vol % garnet to 0.045 g cm^{-3} for 90 vol % garnet.

5.4 Delamination in Tibet

The development of delamination is associated with the instability of the lower crust and the mantle lithosphere. The eclogitization of the subducted slab and lower crust plays a vital role in the process of delamination due to the high density of eclogite, which makes the formation denser than the surrounding mantle lithosphere and provides critical negative buoyancy (Göğüş and Ueda, 2018; Krystopowicz and Currie, 2013). The densities of the eclogitic lower crust and mantle

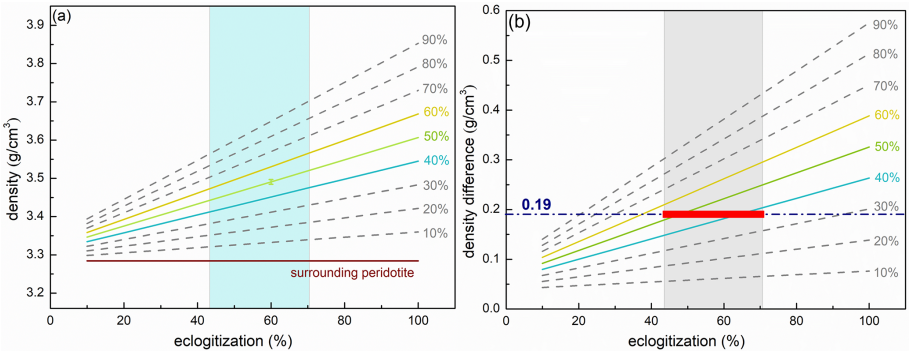

Figure 6. **(a)** The effect of eclogitization on the density of the subducted slab at ∼ 80 km (2.6 GPa and 625 °C) along the Paleozoic geothermal line. The percentage on the right represents the content of garnet, and the content of epidote is fixed at 5 vol % by default. The content of garnets in Tibet is between 40 vol % and 60 vol %. The density represents the average density of the subducted slab with the entire eclogitic ocean lower crust and partially eclogitized lithospheric mantle; the degree of eclogitization refers to the lithospheric mantle. The rufous line represents the average density of surrounding peridotite in this study. The blue shading indicates the possible degree of eclogitization. **(b)** Density difference between eclogite with different degrees of eclogitization and surrounding peridotite. The red dashed solid line represents a density excess of 0.19 g cm^{-3} from the isostatic balance and the geoid anomaly (Matchette-Downes et al., 2019).

lithosphere during slab subduction and convective removal are sufficiently higher than that of the asthenosphere and are good candidates for the initiation of destabilization.

5.4.1 Subducted slab break-off

A series of collisional break-off events is proposed to have occurred throughout 60–45 Ma in Tibet (Chung et al., 2005, 2009; Ma et al., 2014; Zhu et al., 2015). The formation of eclogite presumably kick-starts slab break-off during the subduction of the Indian oceanic plate underthrust below the southern margin of Tibet. The subducted Indian oceanic slab fragmented into several pieces due to what has been identified as a high-velocity anomaly (Peng et al., 2016; Y.-N. Shi et al., 2020). The seismological evidence of high density (Hetényi et al., 2007), high V_P (Schulte-Pelkum et al., 2005), and low longitudinal to transverse (V_P/V_S) ratios (Wittlinger et al., 2009) further confirms that there may be variable degrees of eclogitization beneath Tibet. Figure 6 shows the density profile of subducted slabs with different garnet compositions, different degrees of eclogitization, and variable densities compared with the surrounding peridotite. An increasing degree of eclogitization and an enhanced garnet content in eclogite increases the density difference between the slab and the surrounding peridotite. Previous studies have made preliminary estimates of the average density from the isostatic balance and geoid anomalies and postulated that the density excess could be between 0 and 0.19 g cm^{-3} (Matchette-Downes et al., 2019). For Tibetan eclogite containing 40 vol %–60 vol % garnet, if the lithospheric mantle is a mixture of peridotite and eclogite with a density anomaly of 0.19 g cm^{-3}, our model requires a range of 44 %–70 % eclogitization. If the eclogite is high-Fe, only 30 %–48 % eclogitization is needed to produce the density difference (Fig. S12), while eclogitization in the range of 49 %–74 % is needed for the low-Fe eclogite. However, some seismological data show that the crust or lithospheric mantle being only ∼ 30 % eclogitized might cause gravitational instability in Tibet (Matchette-Downes et al., 2019; D. Shi et al., 2020), which is lower than our estimation. Our results clearly show that density excess is closely linked with garnet content and eclogitization degree. If eclogite has a high garnet content, a relatively low degree of eclogitization could instigate the delamination of slab break-off.

On the other hand, the presence of a weak lower crust and a vertical conduit to accommodate asthenosphere influx is also necessary for the delamination process. The weak layer between the residual crustal and downward peeling lithosphere layer (and/or lower crust) (Göğüş and Ueda, 2018) could promote the initiation and propagation of delamination. Therefore, very high temperatures and relatively low lower-crustal viscosities are also other controlling factors of delamination (Göğüş and Pysklywec, 2008; Morency, 2004). Here, we assume that the length of the fractured slab is 60 km, which drops 80 km over 45 Myr, and that the viscosity of the asthenosphere is 5×10^{20} Pa S (Wang et al., 2019). By using Stokes' law (Sect. S3 in the Supplement), ignoring the thermal disturbance, and assuming the most ideal conditions, the density difference caused by eclogite needs to be at least 0.15 g cm^{-3} to produce such delamination. The result is close to those discussed above in gravity anomalies.

In particular, the presence of eclogite with a greater abundance of garnet, a higher Fe content, and a greater degree of eclogitization would instigate the delamination process of slab break-off.

5.4.2 Removal of the eclogitized lower crust

The thickened lower crust undergoes "convective removal" due to gravitational instability, which is another type of delamination that occurred in Tibet from 25 to 0 Ma (Chung et al., 2005; Nomade et al., 2004). The convective removal of the lithosphere during delamination corresponds to higher temperature conditions (Craig et al., 2020). In this circumstance, the density of Tibetan eclogite is 6.9 %–10.8 % denser than the surrounding peridotite at ∼ 60 km (Fig. 5b), which is analogous to the results in the case of subducted slab detachment. This result is also in ample agreement with the result obtained by Garber et al. (2018), which noted that eclogite is 5 %–10 % denser than peridotite. The density difference between eclogite and peridotite is 0.22–0.35 g cm^{-3} with 40 vol %–60 vol % garnet in Tibet (Fig. 5d). During this stage, it is believed that delamination of the thickened, eclogitized lower crust occurred. Similarly, Stokes' law can be used considering ideal conditions without any thermal disturbance. If the falling block is assumed to be approximately 30 km in the longitudinal direction and the viscosity of the asthenosphere is 5×10^{20} Pa S, the falling block can drop by 70–110 km within 25 Myr. For eclogite with a high Fe content, a density difference of 0.35–0.50 g cm^{-3} makes the fragmented block capable of falling 105–155 km, while the density difference of 0.24–0.33 g cm^{-3} with a low Fe content makes the block able to fall 75–102 km (Fig. S13 in the Supplement). The fragmented block with a high Fe content can fall a larger distance at the same time, indicating that the high Fe content is more likely to promote the occurrence of delamination. This result is consistent with the high-velocity anomalous blocks identified at 100–200 km by seismic tomography (Peng et al., 2016; D. Shi et al., 2016, 2020).

In summary, density contrasts can provide a stimulus for the initiation of instability. It is accepted that eclogite with a high garnet content and a high Fe content as well as a high proportion of eclogite in the lithospheric mantle may have strongly promoted delamination during the process of India–Asia collision from the perspective of density.

6 Conclusions

The P–V–T EoS of the main minerals of eclogite is combined with its mineral composition and the geothermal line to derive the density of Tibetan eclogite in this study. We offer a new perspective by obtaining the thermal EoS for the main minerals of eclogite in a single experiment. The thermal EoS parameters of the main minerals of eclogite are derived by fitting the P–V–T data to the HT-BM-EoS. The density of minerals along the Tibetan geotherm shows that the density is closely related to its composition and thermal EoS parameters. Increasing iron contents increase the density of minerals, but if the molecular masses of two minerals are similar, the thermal EoS parameters play a pivotal role. The garnet content profoundly increases the density of eclogite. For every 10 vol % increase in garnet, the density of eclogite increases by approximately 1.7 %. The density of Tibetan eclogite is approximately 7 %–11 % denser than that of the surrounding peridotite. An increasing proportion of garnet, Fe content, and degree of eclogitization enhances the density difference to facilitate the delamination process. For Tibetan eclogite containing 40 vol %–60 vol % garnet, 44 %–70 % eclogitization can produce the same density difference as obtained by the isostatic balance and the geoid anomaly. According to a rough calculation, the fragmented block will fall 70–155 km. A high Fe content is more likely to promote delamination. Eclogite is a good candidate for the initiation of instability and may be more susceptible to inducing the break-off of the subducted slab or the gravitational removal of the lower crust during the process of the India–Asia collision.

Data availability. All the data presented in this paper are available upon request.

Supplement. The Supplement contains the density profile of garnet at high temperature, density profile along the Cenozoic geothermal line, data on unit cell parameters of eclogite minerals, thermal EoS parameters of this study and previous research, figures of Eulerian finite stain-normalized pressure (F_E-f_E), isothermal bulk modulus (K_{T0}) and its pressure derivative (K'_{T0}) plot of garnet and omphacite, normal distribution of eclogite minerals, density evolution of minerals, and density profile of eclogite with different Fe contents. The supplement related to this article is available online at: https://doi.org/10.5194/se-13-745-2022-supplement.

Author contributions. All authors contributed to the preparation and revision of the paper. ZY contributed to data curation, investigation, formal analysis, and writing (original draft, review, and editing). DF contributed to investigation, conceptualization, supervision, methodology, funding acquisition, and writing (review and editing). BL contributed to data curation and writing (review and editing). QT contributed to software, validation, and writing (review and editing). JX contributed to investigation, supervision, and writing (review and editing). DZ contributed to formal analysis and writing (review and editing). WZ contributed to investigation, conceptualization, supervision, and writing (review and editing).

Competing interests. The contact author has declared that neither they nor their co-authors have any competing interests.

Disclaimer. Publisher's note: Copernicus Publications remains neutral with regard to jurisdictional claims in published maps and institutional affiliations.

Acknowledgements. We thank editor Florian Fusseis, an anonymous reviewer and two members of the wider scientific community for their thorough reading of our paper and constructive comments, which further improved the quality of our paper. We also acknowledge Sergey N. Tkachev for the gas loading assistance. The diffraction experiments were performed at GeoSoilEnviroCARS (Sector 13-BM-C), Partnership for Extreme Crystallography program (PX^2), Advanced Photon Source (APS), and Argonne National Laboratory.

Financial support. This project was funded by the National Natural Science Foundation of China (grant nos. 42172048, U2032118, and 41802043), the Youth Innovation Promotion Association CAS (Dawei Fan, grant no. 2018434), the Chinese Academy of Sciences "Light of West China" Program (2019), the Guizhou Provincial Science and Technology Projects (QKHJC-ZK[2021]ZD042), and the Innovation and Entrepreneurship Funding of High-Level Overseas Talents of Guizhou Province (Dawei Fan, [2019] 10).

Review statement. This paper was edited by Florian Fusseis and reviewed by one anonymous referee.

References

Angel, R. J., Alvaro, M., and Gonzalez-Platas, J.: EosFit7c and a Fortran module (library) for equation of state calculations, Z. Krist.-Cryst. Mater., 229, 405–419, https://doi.org/10.1515/zkri-2013-1711, 2014.

Arimoto, T., Gréaux, S., Irifune, T., Zhou, C., and Higo, Y.: Sound velocities of $Fe_3Al_2Si_3O_{12}$ almandine up to 19 GPa and 1700 K, Phys. Earth Planet. In., 246, 1–8, https://doi.org/10.1016/j.pepi.2015.06.004, 2015.

Beyer, C., Kurnosov, A. V., Ballaran, T. B., and Frost, D. J.: High-pressure and high-temperature single-crystal X-ray diffraction of complex garnet solid solutions up to 16 GPa and 823 K, Phys. Chem. Miner., 48, 17, https://doi.org/10.1007/s00269-021-01139-5, 2021.

Birch, F.: Finite Elastic Strain of Cubic Crystals, Phys. Rev., 71, 809–824, https://doi.org/10.1103/PhysRev.71.809, 1947.

Bird, P.: Initiation of intracontinental subduction in the Himalaya, J. Geophys. Res.-Sol. Ea., 83, 4975–4987, https://doi.org/10.1029/JB083iB10p04975, 1978.

Bird, P.: Continental delamination and the Colorado Plateau, J. Geophys. Res.-Sol. Ea., 84, 7561–7571, https://doi.org/10.1029/JB084iB13p07561, 1979.

Chan, G. H. N., Waters, D. J., Searle, M. P., Aitchison, J. C., Horstwood, M. S. A., Crowley, Q., Lo, C. H., and Chan, J. S. L.: Probing the basement of southern Tibet: evidence from crustal xenoliths entrained in a Miocene ultrapotassic dyke, J. Geol. Soc. London, 166, 45–52, https://doi.org/10.1144/0016-76492007-145, 2009.

Chen, W. and Tenzer, R.: The application of a gravimetric forward modelling of the lithospheric structure for an estimate of the average density of the upper asthenosphere, Geod. Geodyn., 10, 265–275, https://doi.org/10.1016/j.geog.2019.04.003, 2019.

Cheng, H., Liu, Y., Vervoort, J. D., and Lu, H.: Combined U-Pb, Lu-Hf, Sm-Nd and Ar-Ar multichronometric dating on the Bailang eclogite constrains the closure timing of the Paleo-Tethys Ocean in the Lhasa terrane, Tibet, Gondwana Res., 28, 1482–1499, https://doi.org/10.1016/j.gr.2014.09.017, 2015.

Chung, S.-L., Chu, M.-F., Zhang, Y., Xie, Y., Lo, C.-H., Lee, T.-Y., Lan, C.-Y., Li, X., Zhang, Q., and Wang, Y.: Tibetan tectonic evolution inferred from spatial and temporal variations in post-collisional magmatism, Earth-Sci. Rev., 68, 173–196, https://doi.org/10.1016/j.earscirev.2004.05.001, 2005.

Chung, S.-L., Chu, M.-F., Ji, J., O'Reilly, S. Y., Pearson, N. J., Liu, D., Lee, T.-Y., and Lo, C.-H.: The nature and timing of crustal thickening in Southern Tibet: Geochemical and zircon Hf isotopic constraints from postcollisional adakites, Tectonophysics, 477, 36–48, https://doi.org/10.1016/j.tecto.2009.08.008, 2009.

Conrad, C. P. and Molnar, P.: Convective instability of a boundary layer with temperature-and strain-rate-dependent viscosity in terms of "available buoyancy", Geophys. J. Int., 139, 51–68, https://doi.org/10.1046/j.1365-246X.1999.00896.x, 1999.

Craig, T. J., Kelemen, P. B., Hacker, B. R., and Copley, A.: Reconciling Geophysical and Petrological Estimates of the Thermal Structure of Southern Tibet, Geochem. Geophy. Geosy., 21, e2019GC008837, https://doi.org/10.1029/2019GC008837, 2020.

DeCelles, P. G., Robinson, D. M., and Zandt, G.: Implications of shortening in the Himalayan fold-thrust belt for uplift of the Tibetan Plateau, Tectonics, 21, 12-1–12-25, https://doi.org/10.1029/2001TC001322, 2002.

Dera, P., Zhuravlev, K., Prakapenka, V., Rivers, M. L., Finkelstein, G. J., Grubor-Urosevic, O., Tschauner, O., Clark, S. M., and Downs, R. T.: High pressure single-crystal micro X-ray diffraction analysis with GSE_ADA/RSV software, High Pressure Res., 33, 466–484, https://doi.org/10.1080/08957959.2013.806504, 2013.

Dong, Y., Xie, C., Yu, Y., Wang, B., Li, L., and Zeng, X.: The discovery of Longyasongduo eclogite from Gongbujiangda County, Tibet, and its significance., Geol. Bull. of China, 37, 1464–1471, 2018.

Ehlers, T. A. and Poulsen, C. J.: Influence of Andean uplift on climate and paleoaltimetry estimates, Earth Planet. Sc. Lett., 281, 238–248, https://doi.org/10.1016/j.epsl.2009.02.026, 2009.

Faccenda, M., Minelli, G., and Gerya, T. V.: Coupled and decoupled regimes of continental collision: Numerical modeling, Earth Planet. Sc. Lett., 278, 337–349, https://doi.org/10.1016/j.epsl.2008.12.021, 2009.

Faccincani, L., Faccini, B., Casetta, F., Mazzucchelli, M., Nestola, F., and Coltorti, M.: EoS of mantle minerals coupled with composition and thermal state of the lithosphere: Inferring the density structure of peridotitic systems, Lithos, 404–405, 106483, https://doi.org/10.1016/j.lithos.2021.106483, 2021.

Fan, D., Xu, J., Wei, S., Chen, Z., and Xie, H.: In-situ high-pressure synchrotron X-ray diffraction of natural epidote, Chin. J. High Press. Phys., 28, 257–261, https://doi.org/10.11858/gywlxb.2014.03.001, 2014.

Fei, Y., Ricolleau, A., Frank, M., Mibe, K., Shen, G., and Prakapenka, V.: Toward an internally consistent pressure scale, P. Natl. Acad. Sci. USA, 104, 9182–9186, https://doi.org/10.1073/pnas.0609013104, 2007.

Finkelstein, G. J., Jackson, J. M., Sturhahn, W., Zhang, D., Alp, E. E., and Toellner, T. S.: Single-crystal equations of state of magnesiowüstite at high pressures, Am. Mineral., 102, 1709–1717, https://doi.org/10.2138/am-2017-5966, 2017.

Garber, J. M., Maurya, S., Hernandez, J., Duncan, M. S., Zeng, L., Zhang, H. L., Faul, U., McCammon, C., Montagner, J., Moresi, L., Romanowicz, B. A., Rudnick, R. L., and Stixrude, L.: Multidisciplinary Constraints on the Abundance of Diamond and Eclogite in the Cratonic Lithosphere, Geochem. Geophy. Geosy., 19, 2062–2086, https://doi.org/10.1029/2018GC007534, 2018.

Gatta, G. D., Merlini, M., Lee, Y., and Poli, S.: Behavior of epidote at high pressure and high temperature: a powder diffraction study up to 10 GPa and 1200 K, Phys. Chem. Miner., 38, 419–428, https://doi.org/10.1007/s00269-010-0415-y, 2011.

Göğüş, O. H. and Pysklywec, R. N.: Near-surface diagnostics of dripping or delaminating lithosphere, J. Geophys. Res., 113, B11404, https://doi.org/10.1029/2007JB005123, 2008.

Göğüş, O. H. and Ueda, K.: Peeling back the lithosphere: Controlling parameters, surface expressions and the future directions in delamination modeling, J. Geodyn., 117, 21–40, https://doi.org/10.1016/j.jog.2018.03.003, 2018.

Gottschalk, M.: Thermodynamic Properties of Zoisite, Clinozoisite and Epidote, Rev. Mineral. Geochem., 56, 83–124, https://doi.org/10.2138/gsrmg.56.1.83, 2004.

Gréaux, S. and Yamada, A.: P–V–T equation of state of $Mn_3Al_2Si_3O_{12}$ spessartine garnet, Phys. Chem. Miner., 41, 141–149, https://doi.org/10.1007/s00269-013-0632-2, 2014.

Guillot, S., Mahéo, G., de Sigoyer, J., Hattori, K. H., and Pêcher, A.: Tethyan and Indian subduction viewed from the Himalayan high- to ultrahigh-pressure metamorphic rocks, Tectonophysics, 451, 225–241, https://doi.org/10.1016/j.tecto.2007.11.059, 2008.

Hao, M., Zhang, J. S., Pierotti, C. E., Ren, Z., and Zhang, D.: High-Pressure Single-Crystal Elasticity and Thermal Equation of State of Omphacite and Their Implications for the Seismic Properties of Eclogite in the Earth's Interior, J. Geophys. Res.-Sol. Ea., 124, 2368–2377, https://doi.org/10.1029/2018JB016964, 2019.

He, Y., Li, S., Hoefs, J., Huang, F., Liu, S.-A., and Hou, Z.: Post-collisional granitoids from the Dabie orogen: New evidence for partial melting of a thickened continental crust, Geochim. Cosmochim. Ac., 75, 3815–3838, https://doi.org/10.1016/j.gca.2011.04.011, 2011.

Hetényi, G., Cattin, R., Brunet, F., Bollinger, L., Vergne, J., Nábělek, J. L., and Diament, M.: Density distribution of the India plate beneath the Tibetan plateau: Geophysical and petrological constraints on the kinetics of lower-crustal eclogitization, Earth Planet. Sc. Lett., 264, 226–244, https://doi.org/10.1016/j.epsl.2007.09.036, 2007.

Hodges, K. V., Hurtado, J. M., and Whipple, K. X.: Southward extrusion of Tibetan crust and its effect on Himalayan tectonics, Tectonics, 20, 799–809, https://doi.org/10.1029/2001TC001281, 2001.

Holland, T. J. B. and Powel, R.: An improved and extended internally consistent thermodynamic dataset for phases of petrological interest, involving a new equation of state for solids, J. Metamorph. Geol., 29, 333–383, https://doi.org/10.1111/j.1525-1314.2010.00923.x, 2011.

Holland, T. J. B., Redfern, S. A. T., and Pawley, A. R.: Volume behavior of hydrous minerals at high pressure and temperature; II, Compressibilities of lawsonite, zoisite, clinozoisite, and epidote, Am. Mineral., 81, 341–348, https://doi.org/10.2138/am-1996-3-408, 1996.

Houseman, G. and McKenzie, D. P.: Numerical experiments on the onset of convective instability in the Earth's mantle, Geophys. J. Int., 68, 133–164, https://doi.org/10.1111/j.1365-246X.1982.tb06966.x, 1982.

Houseman, G. A., McKenzie, D. P., and Molnar, P.: Convective instability of a thickened boundary layer and its relevance for the thermal evolution of continental convergent belts, J. Geophys. Res.-Sol. Ea., 86, 6115–6132, https://doi.org/10.1029/JB086iB07p06115, 1981.

Huang, J., Tian, Z. Z., Zhang, C., Yang, J. J., and Chen, M.: Metamorphic evolution of Sumdo eclogite in Lhasa Block of the Tibetan Plateau: Phase equilibrium in NCKMnFMASHTO System, Geol. China, 42, 1559–1571, 2015.

Jiang, F., Speziale, S., and Duffy, T. S.: Single-crystal elasticity of grossular- and almandine-rich garnets to 11 GPa by Brillouin scattering, J. Geophys. Res.-Sol. Ea., 109, B10210, https://doi.org/10.1029/2004JB003081, 2004.

Jin, X., Zhang, Y.-X., Zhou, X.-Y., Zhang, K.-J., Li, Z.-W., Khalid, S. B., Hu, J.-C., Lu, L., and Sun, W.-D.: Protoliths and tectonic implications of the newly discovered Triassic Baqing eclogites, central Tibet: Evidence from geochemistry, Sr Nd isotopes and geochronology, Gondwana Res., 69, 144–162, https://doi.org/10.1016/j.gr.2018.12.011, 2019.

Klotz, S., Chervin, J.-C., Munsch, P., and Le Marchand, G.: Hydrostatic limits of 11 pressure transmitting media, J. Phys. D Appl. Phys., 42, 075413, https://doi.org/10.1088/0022-3727/42/7/075413, 2009.

Krystopowicz, N. J. and Currie, C. A.: Crustal eclogitization and lithosphere delamination in orogens, Earth Planet. Sc. Lett., 361, 195–207, https://doi.org/10.1016/j.epsl.2012.09.056, 2013.

Levin, L. E.: Structure of the thermal lithosphere and asthenosphere beneath oceans and continents, Geotectonics, 40, 357–366, https://doi.org/10.1134/S0016852106050037, 2006.

Li, B., Xu, J., Zhang, D., Ye, Z., Huang, S., Fan, D., Zhou, W., and Xie, H.: Thermoelasticity and stability of natural epidote at high pressure and high temperature: Implications for water transport during cold slab subduction, Geosci. Front., 12, 921–928, https://doi.org/10.1016/j.gsf.2020.05.022, 2020.

Li, C., van der Hilst, R. D., Meltzer, A. S., and Engdahl, E. R.: Subduction of the Indian lithosphere beneath the Tibetan Plateau and Burma, Earth Planet. Sc. Lett., 274, 157–168, https://doi.org/10.1016/j.epsl.2008.07.016, 2008.

Li, H. and Fang, J.: Crustal and upper mantle density structure beneath the qinghai-tibet plateau and surrounding areas derived from EGM2008 geoid anomalies, ISPRS Int. Geo-Inf., 6, 1–15, https://doi.org/10.3390/ijgi6010004, 2017.

Li, J. X., Fan, W. M., Zhang, L. Y., Ding, L., Sun, Y. L., Peng, T. P., Cai, F. L., Guan, Q. Y., and Sein, K.: Subduction of Indian continental lithosphere constrained by Eocene-Oligocene magmatism in northern Myanmar, Lithos, 348–349, 105211, https://doi.org/10.1016/j.lithos.2019.105211, 2019.

Li, Z.-H., Liu, M., and Gerya, T.: Lithosphere delamination in continental collisional orogens: A systematic numerical study, J. Geophys. Res.-Sol. Ea., 121, 5186–5211, https://doi.org/10.1002/2016JB013106, 2016.

Liu, H., Xiao, Y., Van den Kerkhof, A., Wang, Y., Zeng, L., and Guo, H.: Metamorphism and fluid evolution of the Sumdo

eclogite, Tibet: Constraints from mineral chemistry, fluid inclusions and oxygen isotopes, J. Asian Earth Sci., 172, 292–307, https://doi.org/10.1016/j.jseaes.2018.09.013, 2019.

Liu, Y., Santosh, M., Yuan, T., Li, H., and Li, T.: Reduction of buried oxidized oceanic crust during subduction, Gondwana Res., 32, 11–23, https://doi.org/10.1016/j.gr.2015.02.014, 2016.

Lu, C., Mao, Z., Lin, J., Zhuravlev, K. K., Tkachev, S. N., and Prakapenka, V. B.: Elasticity of single-crystal iron-bearing pyrope up to 20 GPa and 750 K, Earth Planet. Sc. Lett., 361, 134–142, https://doi.org/10.1016/j.epsl.2012.11.041, 2013.

Ma, L., Wang, B.-D., Jiang, Z.-Q., Wang, Q., Li, Z.-X., Wyman, D. A., Zhao, S.-R., Yang, J.-H., Gou, G.-N., and Guo, H.-F.: Petrogenesis of the Early Eocene adakitic rocks in the Napuri area, southern Lhasa: Partial melting of thickened lower crust during slab break-off and implications for crustal thickening in southern Tibet, Lithos, 196–197, 321–338, https://doi.org/10.1016/j.lithos.2014.02.011, 2014.

Matchette-Downes, H., van der Hilst, R. D., Gilligan, A., and Priestley, K.: Seismological constraints on the density, thickness and temperature of the lithospheric mantle in southwestern Tibet, Earth Planet. Sc. Lett., 524, 115719, https://doi.org/10.1016/j.epsl.2019.115719, 2019.

Meng, Y., Weidner, D. J., and Fei, Y.: Deviatoric stress in a quasi-hydrostatic diamond anvil cell: Effect on the volume-based pressure calibration, Geophys. Res. Lett., 20, 1147–1150, https://doi.org/10.1029/93GL01400, 1993.

Milani, S., Nestola, F., Alvaro, M., Pasqual, D., Mazzucchelli, M. L., Domeneghetti, M. C., and Geiger, C. A.: Diamond–garnet geobarometry: The role of garnet compressibility and expansivity, Lithos, 227, 140–147, https://doi.org/10.1016/j.lithos.2015.03.017, 2015.

Milani, S., Angel, R. J., Scandolo, L., Mazzucchelli, M. L., Ballaran, T. B., Klemme, S., Domeneghetti, M. C., Miletich, R., Scheidl, K. S., Derzsi, M., Tokár, K., Prencipe, M., Alvaro, M., and Nestola, F.: Thermo-elastic behavior of grossular garnet at high pressures and temperatures, Am. Mineral., 102, 851–859, https://doi.org/10.2138/am-2017-5855, 2017.

Miller, C., Schuster, R., Klotzli, U., Frank, W., and Purtscheller, F.: Post-Collisional Potassic and Ultrapotassic Magmatism in SW Tibet: Geochemical and Sr-Nd-Pb-O Isotopic Constraints for Mantle Source Characteristics and Petrogenesis, J. Petrol., 40, 1399–1424, https://doi.org/10.1093/petroj/40.9.1399, 1999.

Morency, C.: Numerical simulations of the mantle lithosphere delamination, J. Geophys. Res., 109, B03410, https://doi.org/10.1029/2003JB002414, 2004.

Nábělek, P. I. and Nábělek, J. L.: Thermal characteristics of the Main Himalaya Thrust and the Indian lower crust with implications for crustal rheology and partial melting in the Himalaya orogen, Earth Planet. Sc. Lett., 395, 116–123, https://doi.org/10.1016/j.epsl.2014.03.026, 2014.

Nishihara, Y., Takahashi, E., Matsukage, K., and Kikegawa, T.: Thermal equation of state of omphacite, Am. Mineral., 88, 80–86, https://doi.org/10.2138/am-2003-0110, 2003.

Nomade, S., Renne, P. R., Mo, X., Zhao, Z., and Zhou, S.: Miocene volcanism in the Lhasa block, Tibet: spatial trends and geodynamic implications?, Earth Planet. Sc. Lett., 221, 227–243, https://doi.org/10.1016/S0012-821X(04)00072-X, 2004.

Pandolfo, F., Nestola, F., Cámara, F., and Domeneghetti, M. C.: High-pressure behavior of space group P2/n omphacite, Am. Mineral., 97, 407–414, https://doi.org/10.2138/am.2012.3928, 2012a.

Pandolfo, F., Nestola, F., Cámara, F., and Domeneghetti, M. C.: New thermoelastic parameters of natural C2/c omphacite, Phys. Chem. Miner., 39, 295–304, https://doi.org/10.1007/s00269-012-0484-1, 2012b.

Panza, G. F., Brandmayr, E., and Romanelli, F.: A geophysical perspective on the lithosphere–asthenosphere system from Periadriatic to the Himalayan areas: the contribution of gravimetry, Rend. Lincei, 31, 59–67, https://doi.org/10.1007/s12210-020-00892-z, 2020.

Pavese, A., Diella, V., Pischedda, V., Merli, M., Bocchio, R., and Mezouar, M.: Pressure-volume-temperature equation of state of andradite and grossular, by high-pressure and -temperature powder diffraction, Phys. Chem. Miner., 28, 242–248, https://doi.org/10.1007/s002690000144, 2001.

Peng, M., Jiang, M., Li, Z.-H., Xu, Z., Zhu, L., Chan, W., Chen, Y., Wang, Y., Yu, C., Lei, J., Zhang, L., Li, Q., and Xu, L.: Complex Indian subduction style with slab fragmentation beneath the Eastern Himalayan Syntaxis revealed by teleseismic P-wave tomography, Tectonophysics, 667, 77–86, https://doi.org/10.1016/j.tecto.2015.11.012, 2016.

Qin, F., Wu, X., Wang, Y., Fan, D., Qin, S., Yang, K., Townsend, J. P., and Jacobsen, S. D.: High-pressure behavior of natural single-crystal epidote and clinozoisite up to 40 GPa, Phys. Chem. Miner., 43, 649–659, https://doi.org/10.1007/s00269-016-0824-7, 2016.

Ren, Y. and Shen, Y.: Finite frequency tomography in southeastern Tibet: Evidence for the causal relationship between mantle lithosphere delamination and the north–south trending rifts, J. Geophys. Res., 113, B10316, https://doi.org/10.1029/2008JB005615, 2008.

Rivers, M., Prakapenka, V., Kubo, A., Pullins, C., Holl, C., and Jacobsen, S.: The COMPRES/GSECARS gas-loading system for diamond anvil cells at the Advanced Photon Source, High Pressure Res., 28, 273–292, https://doi.org/10.1080/08957950802333593, 2008.

Robertson, E. C.: Thermal properties of rocks, U.S. Geological Survey, https://doi.org/10.3133/ofr88441, 1988.

Schulte-Pelkum, V., Monsalve, G., Sheehan, A., Pandey, M. R., Sapkota, S., Bilham, R., and Wu, F.: Imaging the Indian subcontinent beneath the Himalaya, Nature, 435, 1222–1225, https://doi.org/10.1038/nature03678, 2005.

Semprich, J., Simon, N. S. C., and Podladchikov, Y. Y.: Density variations in the thickened crust as a function of pressure, temperature, and composition, Int. J. Earth Sci., 99, 1487–1510, https://doi.org/10.1007/s00531-010-0557-7, 2010.

Shi, D., Zhao, W., Klemperer, S. L., Wu, Z., Mechie, J., Shi, J., Xue, G., and Su, H.: West–east transition from underplating to steep subduction in the India–Tibet collision zone revealed by receiver-function profiles, Earth Planet. Sc. Lett., 452, 171–177, https://doi.org/10.1016/j.epsl.2016.07.051, 2016.

Shi, D., Klemperer, S. L., Shi, J., Wu, Z., and Zhao, W.: Localized foundering of Indian lower crust in the India-Tibet collision zone, P. Natl. Acad. Sci. USA, 117, 24742–24747, https://doi.org/10.1073/pnas.2000015117, 2020.

Shi, Y.-N., Niu, F., Li, Z.-H., and Huangfu, P.: Craton destruction links to the interaction between subduction and mid-lithospheric discontinuity: Implications for the east-

ern North China Craton, Gondwana Res., 83, 49–62, https://doi.org/10.1016/j.gr.2020.01.016, 2020.

Singh, A. and Kumar, M. R.: Seismic signatures of detached lithospheric fragments in the mantle beneath eastern Himalaya and southern Tibet, Earth Planet. Sc. Lett., 288, 279–290, https://doi.org/10.1016/j.epsl.2009.09.031, 2009.

Singh, H. and Mahatsente, R.: Lithospheric Structure of Eastern Tibetan Plateau from Terrestrial and Satellite Gravity Data Modeling: Implication for Asthenospheric Underplating, Lithosphere, 2020, 8897964, https://doi.org/10.2113/2020/8897964, 2020.

Skinner, B. J.: Section 6: Thermal expansion, in: Handbook of Physical Constants, Geological Society of America, 75–96, https://doi.org/10.1130/MEM97-p75, 1966.

Song, S. G., Yang, J. S., Xu, Z. Q., Liou, J. G., and Shi, R. D.: Metamorphic evolution of the coesite-bearing ultrahigh-pressure terrane in the North Qaidam, Northern Tibet, NW China, J. Metamorph. Geol., 21, 631–644, https://doi.org/10.1046/j.1525-1314.2003.00469.x, 2003.

Turner, S., Hawkesworth, C., Liu, J., Rogers, N., Kelley, S., and van Calsteren, P.: Timing of Tibetan uplift constrained by analysis of volcanic rocks, Nature, 364, 50–54, https://doi.org/10.1038/364050a0, 1993.

Wang, C., Zhao, X., Liu, Z., Lippert, P. C., Graham, S. A., Coe, R. S., Yi, H., Zhu, L., Liu, S., and Li, Y.: Constraints on the early uplift history of the Tibetan Plateau, P. Natl. Acad. Sci. USA, 105, 4987–4992, https://doi.org/10.1073/pnas.0703595105, 2008.

Wang, C., Chen, W.-P., and Wang, L.-P.: Temperature beneath Tibet, Earth Planet. Sc. Lett., 375, 326–337, https://doi.org/10.1016/j.epsl.2013.05.052, 2013.

Wang, Q., Wyman, D. A., Li, Z. X., Sun, W., Chung, S. L., Vasconcelos, P. M., Zhang, Q. Y., Dong, H., Yu, Y. S., Pearson, N., Qiu, H. N., and Zhu, T. X.: Eocene north–south trending dikes in central Tibet: new constraints on the timing of east, Earth Planet. Sc. Lett., 298, 205–221, https://doi.org/10.1016/j.epsl.2010.07.046, 2010.

Wang, X., Holt, W. E., and Ghosh, A.: Joint modeling of lithosphere and mantle dynamics: Sensitivity to viscosities within the lithosphere, asthenosphere, transition zone, and D" layers, Phys. Earth Planet. In., 293, 106263, https://doi.org/10.1016/j.pepi.2019.05.006, 2019.

Weller, O. M., St-Onge, M. R., Rayner, N., Waters, D. J., Searle, M. P., and Palin, R. M.: U–Pb zircon geochronology and phase equilibria modelling of a mafic eclogite from the Sumdo complex of south-east Tibet: Insights into prograde zircon growth and the assembly of the Tibetan plateau, Lithos, 262, 729–741, https://doi.org/10.1016/j.lithos.2016.06.005, 2016.

Wittlinger, G., Farra, V., Hetényi, G., Vergne, J., and Nábělek, J.: Seismic velocities in Southern Tibet lower crust: a receiver function approach for eclogite detection, Geophys. J. Int., 177, 1037–1049, https://doi.org/10.1111/j.1365-246X.2008.04084.x, 2009.

Xu, J., Zhang, D., Dera, P., Zhang, B., and Fan, D.: Experimental evidence for the survival of augite to transition zone depths, and implications for subduction zone dynamics, Am. Mineral., 102, 1516–1524, https://doi.org/10.2138/am-2017-5959, 2017.

Xu, J., Zhang, D., Fan, D., Zhang, J. S., Hu, Y., Guo, X., Dera, P., and Zhou, W.: Phase Transitions in Orthoenstatite and Subduction Zone Dynamics: Effects of Water and Transition Metal Ions, J. Geophys. Res.-Sol. Ea., 123, 2723–2737, https://doi.org/10.1002/2017JB015169, 2018.

Xu, J., Zhang, D., Fan, D., Dera, P. K., Shi, F., and Zhou, W.: Thermoelastic Properties of Eclogitic Garnets and Omphacites: Implications for Deep Subduction of Oceanic Crust and Density Anomalies in the Upper Mantle, Geophys. Res. Lett., 46, 179–188, https://doi.org/10.1029/2018GL081170, 2019.

Xu, J., Fan, D., Zhang, D., Li, B., Zhou, W., and Dera, P. K.: Investigation of the crystal structure of low water content hydrous olivine to 29.9 GPa: a high-pressure single-crystal X-ray diffraction study, Am. Mineral., 105, 1857–1865, https://doi.org/10.2138/am-2020-7444, 2020a.

Xu, J., Fan, D., Zhang, D., Guo, X., Zhou, W., and Dera, P. K.: Phase Transition of Enstatite-Ferrosilite Solid Solutions at High Pressure and High Temperature: Constraints on Metastable Orthopyroxene in Cold Subduction, Geophys. Res. Lett., 47, 1–10, https://doi.org/10.1029/2020GL087363, 2020b.

Yang, J., Xu, Z., Li, Z., Xu, X., Li, T., Ren, Y., Li, H., Chen, S., and Robinson, P. T.: Discovery of an eclogite belt in the Lhasa block, Tibet: A new border for Paleo-Tethys?, J. Asian Earth Sci., 34, 76–89, https://doi.org/10.1016/j.jseaes.2008.04.001, 2009.

Yang, Y., Abart, R., Yang, X., Shang, Y., Ntaflos, T., and Xu, B.: Seismic anisotropy in the Tibetan lithosphere inferred from mantle xenoliths, Earth Planet. Sc. Lett., 515, 260–270, https://doi.org/10.1016/j.epsl.2019.03.027, 2019.

Ye, Z., Fan, D., Tang, Q., Xu, J., Zhang, D., and Zhou, W.: Constraining the density evolution during destruction of the lithospheric mantle in the eastern North China Craton, Gondwana Res., 91, 18–30, https://doi.org/10.1016/j.gr.2020.12.001, 2021.

Zhai, Q., Zhang, R., Jahn, B., Li, C., Song, S., and Wang, J.: Triassic eclogites from central Qiangtang, northern Tibet, China: Petrology, geochronology and metamorphic P–T path, Lithos, 125, 173–189, https://doi.org/10.1016/j.lithos.2011.02.004, 2011a.

Zhai, Q., Jahn, B., Zhang, R., Wang, J., and Su, L.: Triassic Subduction of the Paleo-Tethys in northern Tibet, China: Evidence from the geochemical and isotopic characteristics of eclogites and blueschists of the Qiangtang Block, J. Asian Earth Sci., 42, 1356–1370, https://doi.org/10.1016/j.jseaes.2011.07.023, 2011b.

Zhang, D., Hu, Y., and Dera, P. K.: Compressional behavior of omphacite to 47 GPa, Phys. Chem. Miner., 43, 707–715, https://doi.org/10.1007/s00269-016-0827-4, 2016.

Zhang, D., Dera, P. K., Eng, P. J., Stubbs, J. E., Zhang, J. S., Prakapenka, V. B., and Rivers, M. L.: High Pressure Single Crystal Diffraction at PX^2, JoVE-J. Vis. Exp., 2017, 1–9, https://doi.org/10.3791/54660, 2017.

Zhao, M.-S., Chen, Y.-X., and Zheng, Y.-F.: Geochemical evidence for forearc metasomatism of peridotite in the Xigaze ophiolite during subduction initiation in Neo-Tethyan Ocean, south to Tibet, Lithos, 380–381, 105896, https://doi.org/10.1016/j.lithos.2020.105896, 2021.

Zhu, D.-C., Wang, Q., Zhao, Z.-D., Chung, S.-L., Cawood, P. A., Niu, Y., Liu, S.-A., Wu, F.-Y., and Mo, X.-X.: Magmatic record of India-Asia collision, Sci. Rep., 5, 14289, https://doi.org/10.1038/srep14289, 2015.

Zou, Y., Gréaux, S., Irifune, T., Whitaker, M. L., Shinmei, T., and Higo, Y.: Thermal equation of state of $Mg_3Al_2Si_3O_{12}$ pyrope garnet up to 19 GPa and 1700 K, Phys. Chem. Miner., 39, 589–598, https://doi.org/10.1007/s00269-012-0514-z, 2012.